

# Modelling and Numerical Simulation During Selective Laser Melting of Stainless Steel 316L Via Particle by Particle Approach

Walaa Isam Rasool<sup>a\*</sup> , Ziad Aeyad Taha<sup>a</sup>

<sup>a</sup>University of Baghdad, Institute of Laser for Postgraduate Studies, Baghdad, Iraq.

Received: October 04, 2023; Revised: December 23, 2023; Accepted: January 25, 2024

Additive manufacturing (AM) technology depends on the implemented selective laser melting (SLM) process. A good comprehension of its parameters is required to perform an efficient SLM process. Therefore, this study develops a computational fluid dynamic (CFD) model to simulate the SLM process based on a novel approach (particle by particle) and analyze its operating parameters. The model is based on the classical physics laws to formulate the governing equations and solve them in the ANSYS FLUENT software WORKBENCH R19.1. Melting of stainless steel 316L powder particles was considered a case study where laser power, scanning speed, and spot diameter were considered steady parameters. A User Define Function (UDF) is written in C-language to define the heat source and its parameters, and then it is run over the cell face center in every time step. A parametric study was conducted for three of the SLM main parameters; laser power, spot diameter, and scanning speed. The model was verified through the validation process, which confirmed the model's accuracy and reliability. The model outcomes revealed a proportional relationship between the laser power and each melting temperature and liquid mass fraction for a fixed spot diameter and scanning speed. Moreover, a higher energy density is achieved for a smaller laser spot diameter, which yields a higher liquid fraction and melt temperature.

**Keywords:** Additive manufacturing, Selective laser melting, computational fluid dynamics, stainless steel 316L, SLM performance parameters.

## 1. Introduction

One of the technologies recently emerging for additive manufacturing (AM) is selective laser melting (SLM). Since it was developed by German scientists in 1995, SLM has attracted increasing interest and has advanced speedily in recent years<sup>1,2</sup>. The two essential methodologies to conduct the SLM are the powder particles laying and melting. The underlying physical concepts behind the SLM technique are quite complex, particularly those related to phase transition, powder spattering, droplet, and evaporation<sup>3</sup>. The literature shows that significant experimental efforts have been done to investigate the SLM technique, where some final product faults like surface defects, porosity, and spatter are reported<sup>4,6</sup>. Other experimental studies considered the effect of the SLM process parameters<sup>7-9</sup> with a special interest in volumetric laser energy density ( $\eta$ )<sup>10,11</sup>; however, this investigation type has proven tough and expensive. On the other hand, numerical techniques have been increasingly employed in recent years as an alternative cost-effective procedure to provide a comprehensive insight into the process. Studies that adopted these techniques provided almost a full understanding of the SLM mechanisms and effectively improved the process performance.

Khairallah et al.<sup>12</sup> used the arbitrary Lagrange Euler (ALE) methodology to present an accurate simulation technique

to investigate how the molten flow produces spattering, defects, and denudation zones. The modeling normally takes the heat source as a normal volumetric heat source<sup>13</sup> or a surface heat source<sup>14</sup>. However, the laser energy absorption is still far from the experimental studies, which suggest that the laser absorptivity is non-homogenous<sup>8</sup>.

Aiming to analyze the thermodynamic mechanism and the porosity evolution, Xia et al.<sup>15</sup> suggested a CFD model with arbitrarily produced powder particles. Both metallurgical and open porosity were considered and reported to be scanning speed dependent.

The computational fluid dynamics (CFD) technique is commonly used to analyze the SLM fundamental operating parameter among many other numerical modeling procedures. In this context, Tang et al.<sup>16</sup> used the CFD to develop a powder-scale model for simulating an object of two layers. The study accredited the occurrence of porosity to the gas entrapment due to the fusion lack, Yan et al.<sup>13</sup> based on DEM and CFD to develop a Multiphysics model for electron beam type selective melting process that is alike the SLM in terms of modeling procedure. Multiphysics was also used by Ansari et al.<sup>17</sup> to suggest a numerical model to examine the variables influencing part production in the SLM process and the corresponding mathematical connections. The analysis utilizes stainless steel 316L powder.

In another study, Bayat et al.<sup>18</sup> considered multi-layer and multi-track cases to develop a model to simulate the creation

\*e-mail: [walaa.isam1101a@ilps.uobaghdad.edu.iq](mailto:walaa.isam1101a@ilps.uobaghdad.edu.iq)

and development of the lack-of-fusion voids. The study employed the DEM process for the powder laying process, whereas the selective melting process was modeled using a heat source model.

An innovative model is developed by Zhang and Zhang<sup>19</sup>; it combines the CFD and the cellular automata (C.A.) to investigate the evolution of the solidification microstructure in a 316L stainless steel fabricated by laser powder bed fusion (LPBF). The developed model suggests that the recoil pressure and the Marangoni force drive melt pool flow. Further, the study reported that the maximum temperature location is at the laser spot center, and the evaporation happens at the laser spot front. Another study by Luo and Zhao<sup>20</sup> provided a model to simulate the temperature field during the SLM process at the part level with efficiency and precision. Efficient simulation was provided track by track and layer by layer. A novel hybrid heat source, merging Gaussian distributed line heat flux and point heat flux, was created in the study to enhance simulation efficiency. The simulation outcomes indicate that the devised simulation approach can effectively and precisely predict the temperature distribution in a component during the process.

Cao<sup>21</sup> used the direct element method (DEM) and the finite-difference method to simulate the formation of a single track. The impact of powder bed tightness, the distribution of particle size, as well as the thickness of lamination were thoroughly investigated. Another numerical model presented by Cao<sup>21</sup> was used to examine the spacing effect of the horizontal direction scanning on the re-melted zone; the study reported a pore reduction when the re-melted zone was increased.

Another study by Liang et al.<sup>22</sup> proposed a computational CFD framework for developing a novel AM for specific alloys. The study combined the CFD-AM with the Phase Diagram Calculation to identify the  $\beta \rightarrow \alpha$  phase transformation location of a Ti-Al-Fe-alloy. The model was validated an X-ray diffraction measurements. The model outcomes confirmed its reliability in predicting the melt pool and determining heat-affected area features. The study concluded that the developed model can be readily applied to evaluate the phase, thermal history, and microstructure. Aiming to analyze the SLM by considering the heat transfer, the solidification, and fluid flow, He et al.<sup>23</sup> developed a multi-physics and multiphase model. The methods of volume-of-fluid and discrete-element were employed to capture the melt-free surface and create the powder bed. The model is focused mainly on characterizing the solidified tracks and molten pool. It also aimed to investigate the neighboring tracks between remolten regions, the laser power, and the scanning spacing effects. To identify appropriate parameters for the SLM process<sup>24</sup>, created a finite element model to simulate the temperature field distribution in parts made from stainless steel 316L. The findings demonstrated that achieving a superior part with a relative density surpassing 99.66% and commendable mechanical properties is possible when utilizing a laser energy density of 119.05 J/mm<sup>3</sup>, a laser power of 200 W, a scanning speed of 700 mm/s, a hatch spacing of 0.08 mm, and a layer thickness of 0.03 mm.

Also, Yu and Zhao<sup>25</sup> also developed a semi-coupled CFD and DEM to analyze a granular media case comprising a

fluid-particle interface and thermally tempted phase changes. The immersed boundary method was employed to analyze the viscous fluid in the solid particles domain. The CFD with a multiphase situation was adopted to consider the gradient of temperature for the granular particle. Moreover, a coupled CFD and DEM technique was implemented to model the solid particles-fluids interactions. A simulation was conducted on a typical powder-based SLM process to validate the model. Then, the model examined three main SLM process parameters; laser energy distribution, laser power, and hatch distance.

Moges et al.<sup>26</sup> proposed a hybrid model for a laser powder bed fusion process using a combination between the measured data and physics-based data, which is anticipated to give precise predictions for the width of the melt pool. Optical images and a CFD model were used to produce a dataset for the melt pool. This data set was then used to develop a hybrid model using Kriging and polynomial regression methods. The investigation of the model performance revealed that it performs well in predicting computational time and accuracy.

Using a Multiphysics model Ansari et al.<sup>17</sup> investigated the parameters' effect on the SLM operation. The investigated parameters include the effect of spot diameter and the laser power on the melt temperature under various scanning velocities. The model was validated using experimentally produced samples produced according to the simulated parameters. The model outcomes revealed that the reason behind the evaporation and unmelted powder imperfections are extreme and insufficient temperatures, respectively. Utilizing FEM, the production of a 316 stainless steel sample was simulated by Kazemi et al.<sup>27</sup>, yielding temperature variations over time and coordinates. Temperature-dependent thermo-physical properties for each phase, encompassing powder, molten, and solid states, were taken into account.

This paper proposes a CFD-based model to simulate the LASER process of stainless steel 316L. The model is dedicated to conducting a parametric analysis for three main parameters affecting the process: the spot diameter, laser power, and scanning velocity. To confirm the model's accuracy and reliability, a validation process was conducted using computational data available in the literature.

## 2. Physical Background Aspects

The SLM process generates three-dimensional parts using a controlled laser beam scanning; the pre-spread powder is selectively melted in a layer-by-layer routine<sup>28</sup> where complex and dimensional precision components with high surface integrity can be produced. The melt pool's sophisticated chemical and physical behavior and the laser processing technique greatly influence the processed parts' microstructure. Combining the SLM's nonequilibrium metallurgy with the material incremental manufacturing (MIM) strategy created a novel technology to produce bulk components from micromaterials. The SLM's main objective is to improve the microparticle dispersion homogeneity and the associated densification response.

The surface evaporation onset dictates the melt pool transition at high laser energy due to high temperature. According to King et al.<sup>29</sup>, the recoil momentum is generated that deforms the gas/melt flat interface and create a deeper

cavity as the laser energy increase. Accordingly, the shallow cavity captures less energy than a deeper one. However, the absorbance is highly correlated to the metal absorptivity. Thus, the geometry of the melt pool turns from flat and wide to deep and narrow.

### 3. Model Description

The classical physics laws that rule the fluid flow were used to formulate the model governing equations solved throughout the numerical simulation. These equations include the conservation of mass, the first and most significant. The second is based on Newton's second law, change of momentum, and the third one is solved by including a thermal gradient in a fluid domain derived from the first law of thermodynamics, energy conservation<sup>30</sup>.

The finite volume method (FVM) is the main discretization method used in the CFD code. This method uses the conservation law formula to write the fluid governing equations. It is important to present that within the CFD code, the case of the fluid can be solved even steadily or unsteadily with an iterative technique. First, an approximate guess value is normally taken for the fluid variables; then, these values are updated within the solution until the convergence. This term of convergence indicates that there will be no further change in the next iteration of the processing of the variable. In this current work, additive manufacturing simulation was performed by considering the laser as a heat source to melt the metal particles. ANSYS FLUENT software is used for solving this case. It includes a Pressure-Based Solver to solve the mass and momentum equations below<sup>31</sup>. The Pressure-Based Solver relies on pressure to perform the CFD and to solve the Navier-Stokes equations. It employs an algorithm that falls under a category known as the projection method. In this method, the velocity field's continuity constraint, which is the conservation of mass, is attained by resolving an equation for pressure.

#### 3.1. Governing equations

As a numerical technique, CFD is used to solve the governing equations of fluid dynamics and partial differential equations. Once discretized on a mesh, they become algebraic equations that can be solved through a finite-difference/finite-volume algorithm. The equations that govern fluid flow for a Newtonian substance and describe the preservation of mass, momentum, and energy in Cartesian coordinate systems are expressed as follows.

##### 3.1.1. Continuity equation

The continuity equation is given by Versteeg and Malalasekera<sup>32</sup>:

$$\frac{\partial \rho}{\partial t} + \frac{\partial(\rho u)}{\partial x} + \frac{\partial(\rho v)}{\partial y} + \frac{\partial(\rho w)}{\partial z} \quad (1)$$

here,  $\rho$  is the fluid density,  $t$  is the time in seconds, and  $u$  is the velocity vectors for  $u$ ,  $v$ , and  $w$  velocity components in the  $x$ ,  $y$ , and  $z$ -directions in meters per second. As we assumed above, the case is being solved based on a pressure-based solver with an incompressible fluid, so the density has a constant value indicating zero change in density.

##### 3.1.2. Navier–Stokes equation

This is an important equation in the CFD code; it represents the term of viscous stress in the balanced form of momentum; the below equation is for momentum in the  $x$ -direction and can be rewritten in the  $y$ - and  $z$ - directions<sup>32</sup>. As can be noticed from the below equation, there is a link between the viscous stress and the pressure on the fluid.

$$\frac{\partial \rho u}{\partial t} + \text{div}(\rho u u) = -\frac{\partial p}{\partial x} + \text{div}(\mu \text{grad } u) + S_{Mx} \quad (2)$$

Equation 2 represents the momentum in the  $x$ -direction, where  $p$  is the pressure,  $\mu$  is the viscosity of the fluid, and  $S$  is the source term, normally this equation is rewritten in a general form as shown below<sup>32</sup>:

$$\rho u \cdot \nabla u = -\nabla p + \nabla \cdot \tau \quad (3)$$

where  $\tau$  is the shear stress tensor and  $\nabla$  denotes  $\frac{\partial}{\partial x} + \frac{\partial}{\partial y} + \frac{\partial}{\partial z}$

##### 3.1.3. The energy equation

The energy equation is given by Versteeg and Malalasekera<sup>32</sup> as:

$$u \frac{\partial T}{\partial x} + v \frac{\partial T}{\partial y} = \alpha_{eff} \left( \frac{\partial^2 T}{\partial x^2} + \frac{\partial^2 T}{\partial y^2} \right) \quad (4)$$

The average heat transfer coefficient ( $\alpha$ ) can be considered based on the total surface area<sup>32</sup>.

##### 3.1.4. Heat distribution equation

A volumetric heat source<sup>33</sup> is proposed to contribute to the laser beam penetration into the powders. This involves both powder surface and penetration directions. The absorptivity profile group is used in the model; it is a volumetric Gaussian distribution that includes the laser beam penetration into the powder<sup>34,35</sup>.

$$Q_{Laser} = \frac{I_0}{b} \exp\left(\frac{-2r^2}{r_0^2}\right) \exp\left(\frac{z-z_0}{b}\right) \quad (5)$$

$$I_0 = \frac{2P}{\pi r_0^2} \quad (6)$$

where  $I_0$  is the laser beam intensity ( $W/m^2$ ),  $b$  is the laser beam penetration distance (m),  $r$  denotes the distance from the beam center to the irradiated point (m),  $r_0$  is the laser beam radius (m),  $z$  is the powder vertical position (m),  $z_0$  is the top of powder position (m), and  $P$  indicates the power of the beam (W)<sup>12</sup>.

It is well established that ANSYS FLUENT software is limited in some cases that need to customize some functions or equations required during the simulation processes. Also, some cases need to calculate according to particular equations every time steps or loops over cell faces. FLUENT is limited in doing that; hence a User Define Function (UDF) was used to solve this issue. The UDF is a C-language code

**Table 1.** Stainless steel 316L properties<sup>38</sup>.

Material Property	Symbol	Value	Unit
Melting Temperature	$T_m$	1650	K
Melting Interval	$\delta T$	$\pm 10$	K
Evaporation Temperature	$T_{ev}$	3086	K
Latent Heat of Melting	$H_m$	$2.8 \times 10^5$	J/kg
Latent Heat of Evaporation	$H_{ev}$	$6.1 \times 10^6$	J/kg
Density	$\rho$	7700 (solid) – 8000 (liquid)	kg/m <sup>3</sup>
Thermal Conductivity	$k$	$11.82 + 1.06 \times 10^{-2}T$	W/m·K
Specific Heat Capacity	$C_p$	$330.9 + 0.563 T - 4.015 \times 10^{-4}T^2 + 9.465 \times 10^{-8} T^3$	J/kg·K
Absorption Coefficient	$A$	0.55 (solid)–0.3 (liquid)	–
Marangoni Coefficient	$dy/dT$	$-0.40 \times 10^{-3}$	N/m·K

compiled and interpreted during the simulation. Once it is interpreted, the function specified for defining the boundary condition or applying the properties of the material, or setting the heat flux will be available in the graphical interface of FLUENT<sup>36</sup>. Therefore, in this current work, the laser heat source with all parameters mentioned in Equations 5 and 6 have been included in the UDF, and it was run over the cell face center every time.

The turbulence model is the computational procedure widely used to understand the importance and effect of fluid turbulence behavior on the mean flow. In the CFD code, there are many turbulence models to solve. It has been documented that the  $k$ - $\epsilon$  model represents the relationship between two-main terms in the fluid flow problems: kinetic energy and the dissipation rate. This model proves the ability to link the mechanism effect of that two-term kinetic energy ( $k$ ) and the dissipation rate of this energy ( $\epsilon$ )<sup>30,37</sup>.

### 3.2. Geometry and mesh generation

The model geometry was created in WORKBENCH R19.1, the design modeler software which prepared the model for the next steps: meshing and solving. The sketch of the prepared CAD model is presented in Figure 1. A two-dimensional CFD model simulates the metal powder–laser interaction. The model was prepared with a transient option to consider a time-dependent solution. The average diameter of the stainless steel 316L particles was 40  $\mu\text{m}$ . The metal powder particles are assumed to be homogeneous circles, and they are assumed to be homogeneously distributed on the plate. The model dimension is 440  $\mu\text{m}$  width and 160  $\mu\text{m}$  thickness, as shown in Figure 1.

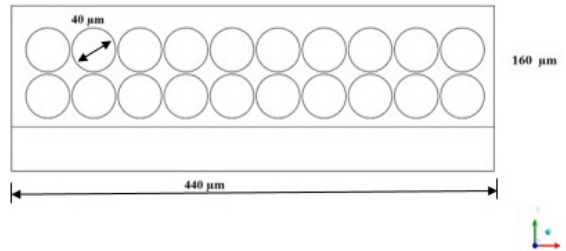
The used S.S. 316L materials properties and their temperature dependence are given in Table 1.

When the model geometry was defined, it was sent to the meshing software, and an unstructured mesh was generated with four grids to conduct a mesh study. A relevant auto mesh factor was set to have four values; 25, 50, 75, and 100; as shown in Table 2, the average cell size was set to 0.003 mm; the mesh graph is given in Figure 2.

This study operates under certain assumptions, including that the melted powder in the melted pool is an incompressible fluid with a Newtonian flow. The flow is

**Table 2.** The mesh independence study.

Grid No.	Total number of cells	Temperature (K)	Mass fraction
1	2300	1966	0.93
2	3052	1840	0.65
3	4624	1637	0.36
4	10836	1674	0.35

**Figure 1.** Model geometry used for the validation process and mesh study.

assumed to be laminar, with a transient flow to capture data on the melting flow field over time. Additionally, the study utilizes a 2D model with a flat surface for the melting pool. These assumptions have been previously recommended<sup>23,39,40</sup>, particularly a 2D model, as the literature suggests that the 3D model is complex and the melted spherical powder behaves symmetrically. Additionally, the evaporation effect was not taken into account, and the analysis only considered convection heat transfer between powder particles and their surroundings. Other thermophysical properties were assumed to be temperature-dependent and homogeneously isotopic.

### 3.3. Mesh independent study

The four grid cases were performed until no divergence in the simulation data due to mesh was achieved. For all cases, it has been determined that the maximum aspect ratio is less than 4, where 1 is perfect, and the minimum orthogonal quality is approximately 0.45. These values are considered more than acceptable and close to the perfect

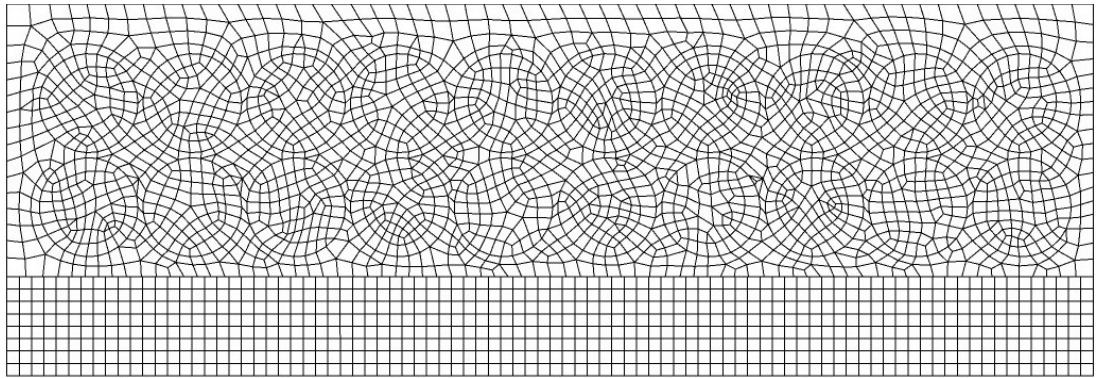


Figure 2. The shape of the used mesh.

value documented in the ANSYS manual<sup>41</sup>. The data given in Table 2 shows the mesh independence study.

From the mesh steady results, it can be noticed that grids No.1 and 2 have significant differences. The predicted temperature is higher when compared to the SS316L melting temperature in Table 1. On the other hand, for grids No.3 and 4, the predicted temperature is so close to that given in Table 1. The error difference between grid No.3 and No.4 is less than 3%. Therefore, grid No.3 was considered for all the cases in this work. It has almost half the number of cells compared to grid No.4, significantly reducing the computational time.

### 3.4. Solver setting

This section explains the ANSYS Fluent solver setting, which comprises the boundary conditions, solution method, and convergence. As for the ANSYS Fluent solver, the first step to be set is whether the solution is a steady or transient state (time dependents). Next, the gravity factor was chosen, where the incompressible fluid flow option was selected because the density of the fluid is constant. Material is an important factor that has to be set; in this case, S.S. 316L has been chosen and set with its properties. The turbulence model with  $K - \epsilon$  was set in this model, as mentioned earlier.

Boundary conditions are another key factor in fluid flow modeling due to their significant effect on the model solution and results. Also, boundary conditions represent the physical model in which the inlet and outlet of the flow are set with which part is stationary or moving part. In this simulation, the entire domain walls were set as fixed walls with slip conditions; this means that the fluid near the first cell adjacent to the wall has a velocity value equal to the main flow velocity. As for the solution method, the Semi-Implicit Method for Pressure-Linked Equations (SIMPLE) was chosen in this study using the pressure velocity coupling algorithms. These algorithms have been utilized to compute the pressure from the momentum and the continuity equations consequently.

The simulation is run for each case with  $5e-06$  time step size with a total of 30-number of time steps and 20 iterations per time step with an assumed turbulent standard  $k$ -epsilon model.

Mentoring the convergence is important; it has been widely used to state whether the solution meets the convergence criteria of the parameters that have been solved in the solver.

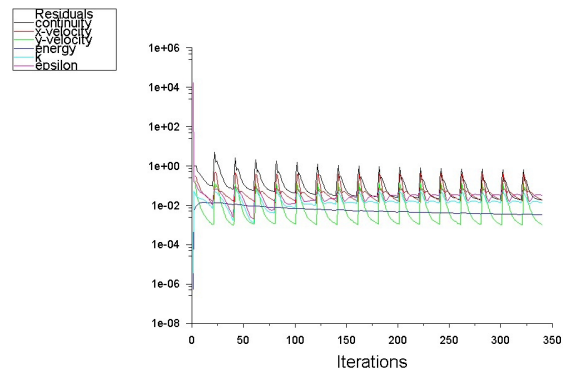


Figure 3. Solution residual plot.

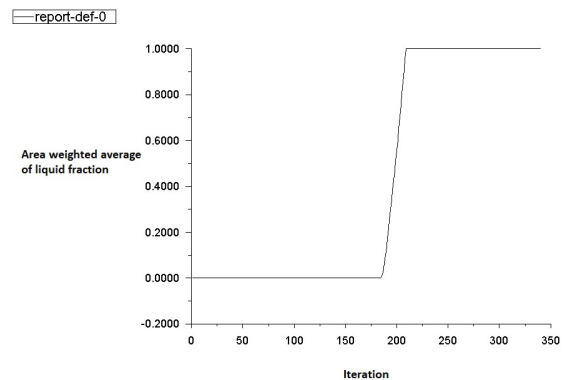


Figure 4. Convergence plot for liquid fraction value with iteration that specified at point ( $x=-0.955$  and  $y= 0.055$  mm) in the domain.

Generally speaking, the first option to be set is monitoring the residual continuity, momentum, and turbulence factors. However, it could not provide the right choice to decide the solution convergence; the monitoring plot of the residual is shown in Figure 3.

The plot in Figure 4 uses the moment to monitor the convergence; the mass fraction was set to be a convergence criterion at the interest area in the first layer of the stainless steel particles. One of the important steps during any simulation is assessing the situation convergence for transit

**Table 3.** The error percentage between the currently predicted results and data provided by Ansari et al.<sup>17</sup>.

Case No.	Laser power (W)	Temperature (K) Ansari et al. <sup>17</sup>	Temperature (K) Current work	Diff. (%)
1	60	2100	2240	6.7
2	75	2300	2397	4.2
3	90	2550	2400	6
4	110	2750	2622	7

or steady-state solution. The default residual plot cannot provide the convergence of the solution correctly, as can be seen; from the graphs, it is difficult to say whether the solution is convergent or not. Therefore, in this study, the convergence of the solution was checked in the area of interest. A point was created at the end of the first circle in the geometry ( $x=-0.955$  and  $y=0.055$  mm), and the liquid fraction was monitored at this point during the solution until the variation in the liquid fraction value became less than 1% per iteration. Figure 4 shows that after 250 iterations, there are no further changes during the solution, which gives us an indication of the convergence of the solution.

#### 4. Model Validation

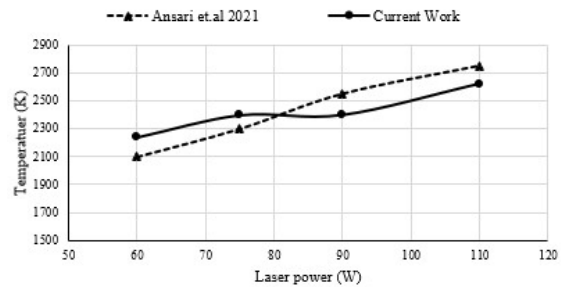
To validate the accuracy and reliability of the developed model, we started the analysis by replicating experimental data presented by Ansari et al.<sup>17</sup> to prove that the model is realistic in predicting the physical properties that need to be investigated. The melt-pool temperature was used as a validation parameter, and the process parameters (laser powers and spot diameter) were taken the same as that given in the experimental investigations<sup>17</sup>. Figure 5 compares the current study prediction of the melt pool temperature and the data achieved experimentally by Ansari et al.<sup>17</sup>. This temperature was obtained at a laser scanning speed of 0.6 m/s and a laser spot diameter of 80  $\mu\text{m}$ . Table 3 lists the plotted data and provides the error percentage between the two sets.

Figure 6 provides the geometrical location (lines a-a) where the validated melt pool temperature is calculated. This line is also used as a position for all the parametric studies conducted in the subsequent sections.

#### 5. Parametric Study

##### 5.1. Laser power

Laser power is a key parameter in the SLM process on which the melt pool temperature and the liquid mass fraction are significantly dependent. Recent studies have highlighted a substantial correlation between the microhardness and tensile strength of samples produced via SLM and the applied laser power<sup>42</sup>. The ongoing simulation is conducted to assess the impact of laser power on the liquid volume fraction in the SLM process. Five distinct laser powers (30, 35, 40, 45, 50 W) were investigated, maintaining a constant scanning velocity of 40 mm/s and a laser spot diameter of 0.025 mm. Figure 7 demonstrates the mass fraction of five different laser power, constant scanning speed, and spot diameter. It shows fitted curves of the mass fraction



**Figure 5.** A comparison between the predicted and measured melt-pool temperature at a laser scanning speed of 0.6 m/s and laser spot diameter of 80  $\mu\text{m}$ .

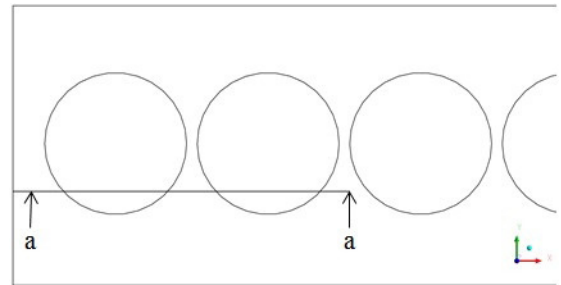


**Figure 6.** Line a-a represents the geometrical location where the validation process and parametric studies are conducted.

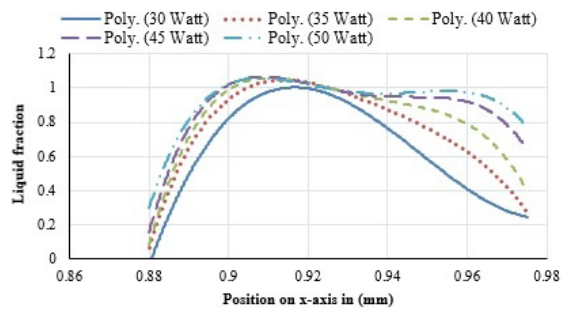


**Figure 7.** Predicted melt-pool liquid fraction at various laser power using scanning velocity of 40 mm/sec and laser spot diameters of 0.025 mm.

distribution along the x-axis and extracted from lines a-a in Figure 6. The results confirm that the relationship between laser power and the mass fraction is proportional. Figure 8 demonstrates the liquid mass fraction contours

obtained at two laser power values, 30 and 50 Watts which are the minimum and maximum power considered for this

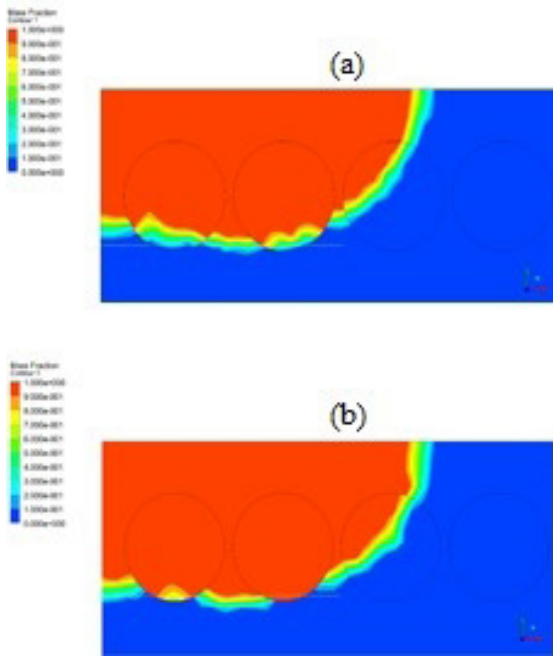


**Figure 8.** Mass fraction contour was used to extract the data; (a) 30 watts laser power, (b) 50 watts laser power with a 40 mm/s scanning speed, and 0.025 mm laser spot diameter.

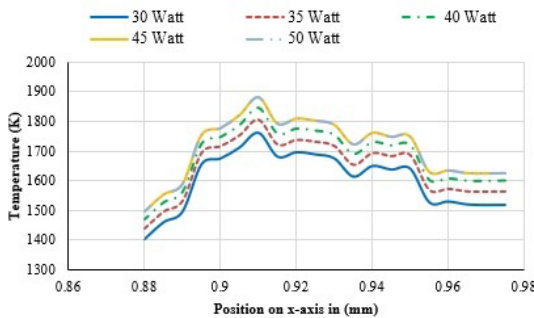


**Figure 9.** Predicted values of melt-pool temperature in K at various laser power, laser spot diameters of 0.025 mm, and laser scanning velocity of 40 mm/sec.

study. It can be seen that at the lower power, no complete melting was achieved for the first and second powder particles. Though, at the higher power, the first and second particles were fully melted, and almost half of the third particle was covered by the liquid.

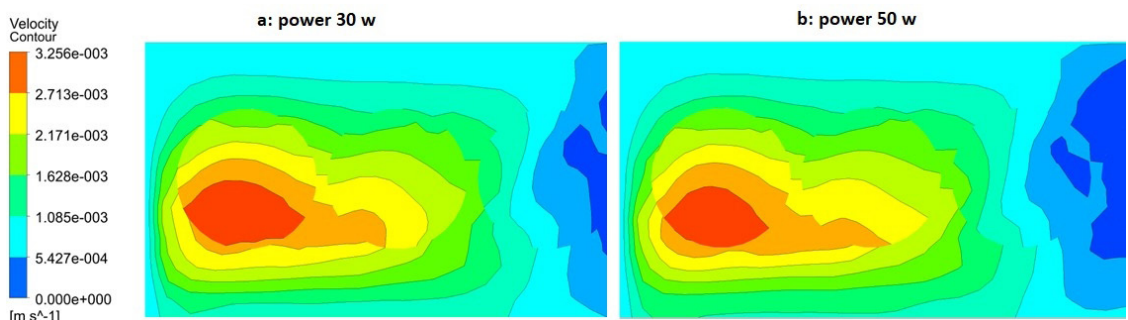
As mentioned earlier in the solver setting, the model was run for each case with a 5e-06-time step size with a total of 30- number of time steps and 20 iterations per time, which means the time for each case is considered fixed for a particular period. Therefore, the liquid fraction reaches the melting phase with a 0.88 value, as these figures show.

Figure 9 illustrates the effect of the laser power on the melt-pool temperature at 40 mm/s laser scanning speed and 0.025 mm laser spot diameter. The given temperature profiles, extracted from the temperature contours, are given along line a-a.

In order to investigate the dynamic behavior of melt pools with laser powers of 30 and 50 W, the velocity field of the melt pool is shown in Figure 10. The blue area on the right side of the figure represents the solidus area where the laser failed to reach the powder, while the left area shows how the metal powders were melted and agitated in vortex shapes. This result has been reported previously by the literature as in He et al.<sup>23</sup>, and the temperature profile and mass fraction results have further confirmed these velocity results. The melted powder moves from the top to the bottom of the plate. In addition, the dimensions of the weld pool do not change isotropically when the laser power changes. The depth-to-width ratio of the melt pool increases, indicating that the effective heat transfers increase more in the vertical direction than in the horizontal direction, as indicated by the red and orange colours.

### 5.2. Scanning speed

Figure 11 and Figure 12 demonstrate the effect of the laser scanning speed on the liquid fraction and melt-pool temperature, respectively, for 30 W laser power and 0.025 mm spot diameter. Five scanning speeds were investigated (30, 40, 50, 60, and 70 mm/s), and the given data is extracted along lines a-a in the x-axis. At each scanning speed, the liquid volume fraction and temperature were obtained after a steady state was achieved. The figures show a reduction in the liquid volume fraction and the temperature of the melt pool as the scanning speed increases. For the best melting process, the power should be enough to melt the new powder



**Figure 10.** Velocity field of a molten pool at laser powers values of 30 and 50 W.

layer in addition to the previous layer to bond the new layer to the prior one.

### 5.3. Laser spot diameter

Figure 13 and Figure 14 depict the effect of the laser spot diameter on the melt-pool liquid fraction and temperature, respectively, for 30 W laser power and 40 mm/sec scanning speed. Five-spot diameters were investigated (0.015, 0.02, 0.025, 0.03, and 0.035 mm), and the given data is extracted along the lines a-a in the x-axis. The energy density concept is

used to justify the melt-pool liquid fraction and temperature. By reducing the laser spot diameter, higher energy density is achieved, yielding higher liquid fraction and melting-pool temperature.

Figure 15 and Figure 16 show the mass fraction contours of three adjacent particles in the S.S. 316L powder for different laser scanning speeds and spot diameters, respectively. Figure 15 depicts the change in liquid mass fraction due to laser scanning speed; it can be noticed that by using 30mm /s laser speed, the mass fraction of the liquid phase

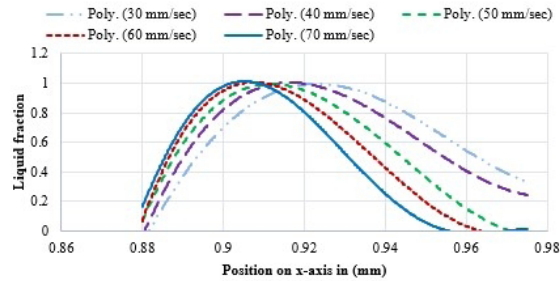


**Figure 11.** Predicted melt-pool liquid fraction at various scanning velocities using 0.025 mm laser spot diameters and 30-watt laser power.

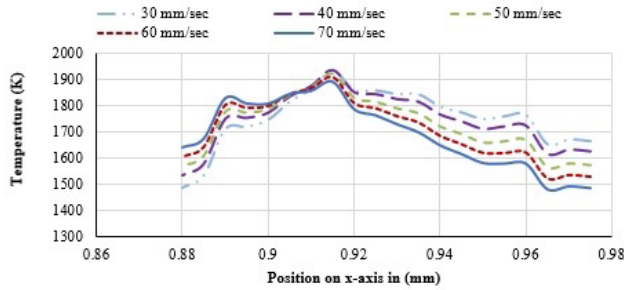


**Figure 12.** Predicted values of melt-pool temperature in K at various scanning velocity, laser spot diameters of 0.025 mm and laser power of 30 watt.

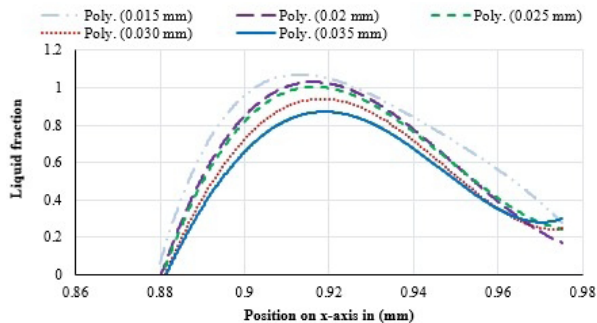


**Figure 13.** Predicted values of liquid fraction (melt-pool) at different spot diameter, laser power of 30 watt and laser scanning velocity of 40 mm/sec.

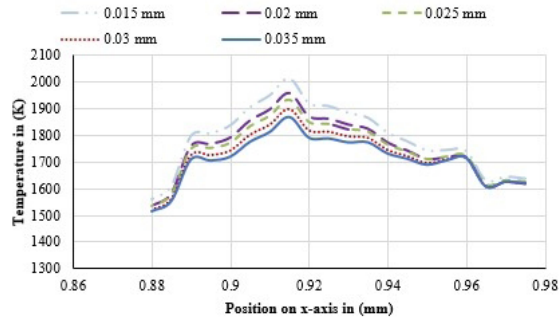


**Figure 14.** Predicted values of melt-pool temperature in K at different spot diameters, laser power of 30 watts, and laser scanning velocity of 40 mm/sec.

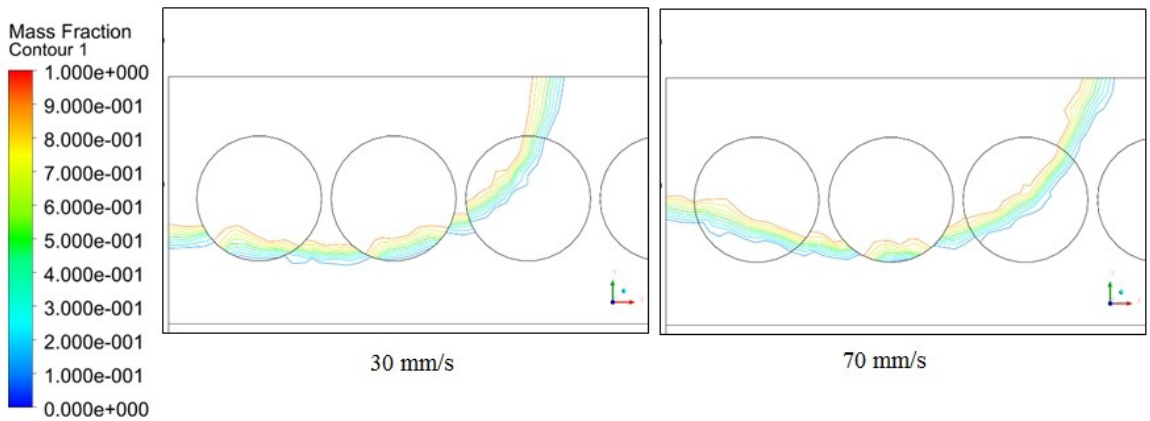


**Figure 15.** The liquid fraction contours for two scanning speeds, 30 and 70 mm/s.

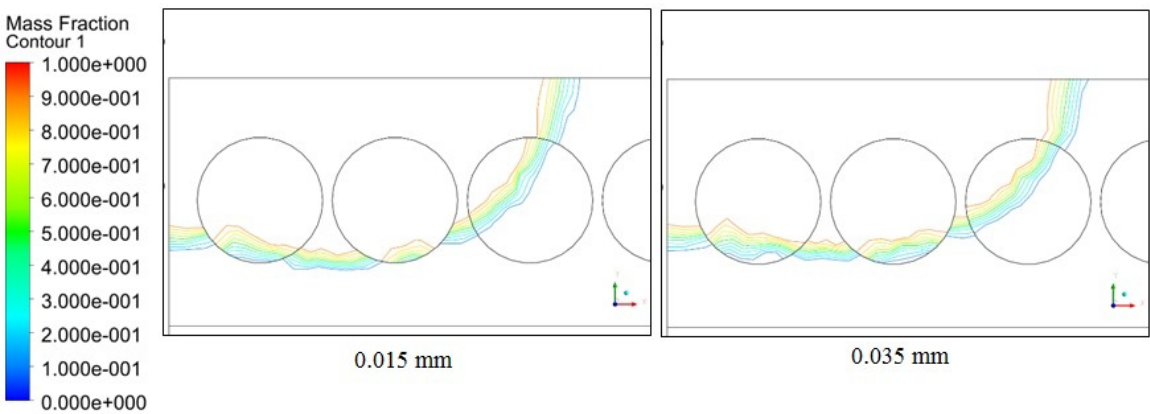


**Figure 16.** The liquid fraction contours for two laser spot diameter, 0.015 and 0.035 mm.

was uniformly distributed on the three particles. On the other hand, in the case of 70 mm/sec scanning speed, the V-shape was formed, which decreases the melting pool.

Figure 16 shows no significant change in the mass fraction when increasing the laser spot diameter from 0.015 to 0.035 mm.

## 6. Conclusions

A CFD model is developed in this study to simulate and analyze the SLM process of the stainless steel 316L powder. The model was developed based on the classical physics laws where the governing equations are formulated and solved

in the ANSYS FLUENT software. A User Define Function (UDF) was written in C-language to define the laser heat source and its parameters; it is run over the cell face center at every step. Our approach novelty can be explained as follows (in the coming points):

- 1- It was considered the shape of the particle (circle) and, for the first time, considered in the modeling of SLM of S.S. 316L.
- 2- This consideration will give a real distribution of temperature during the process.
- 3- The model was verified through validation before a parametric study for three important SLM parameters, laser power intensity, spot diameter, and scanning speed, was conducted. The model outcomes revealed a proportional relationship between the laser power and each melting temperature and liquid mass fraction for a fixed spot diameter and scanning speed. Moreover, the model predicted a higher energy density with a higher liquid fraction and melting temperature for a smaller laser spot diameter.

## 7. References

1. Aboulkhair NT, Simonelli M, Parry L, Ashcroft I, Tuck C, Hague R. 3D printing of Aluminium alloys: additive manufacturing of Aluminium alloys using selective laser melting. *Prog Mater Sci.* 2019;106:100578.
2. Zhang J, Song B, Wei Q, Bourell D, Shi Y. A review of selective laser melting of aluminum alloys: processing, microstructure, property and developing trends. *J Mater Sci Technol.* 2019;35(2):270-84.
3. Markl M, Körner C. Multiscale modeling of powder bed-based additive manufacturing. *Annu Rev Mater Res.* 2016;46(1):93-123.
4. Bidare P, Bitharas I, Ward RM, Attallah MM, Moore AJ. Fluid and particle dynamics in laser powder bed fusion. *Acta Mater.* 2018;142:107-20.
5. Guo Q, Zhao C, Escano LI, Young Z, Xiong L, Fezzaa K, et al. Transient dynamics of powder spattering in laser powder bed fusion additive manufacturing process revealed by in-situ high-speed high-energy x-ray imaging. *Acta Mater.* 2018;151:169-80.
6. Guo Q, Zhao C, Qu M, Xiong L, Hojjatzadeh SMH, Escano LI, et al. In-situ full-field mapping of melt flow dynamics in laser metal additive manufacturing. *Addit Manuf.* 2020;31:100939.
7. Kasperovich G, Haubrich J, Gussone J, Requena G. Correlation between porosity and processing parameters in TiAl6V4 produced by selective laser melting. *Mater Des.* 2016;105:160-70.
8. Guo Q, Zhao C, Qu M, Xiong L, Escano LI, Hojjatzadeh SMH, et al. In-situ characterization and quantification of melt pool variation under constant input energy density in laser powder bed fusion additive manufacturing process. *Addit Manuf.* 2019;28:600-9.
9. Larimian T, Kannan M, Grzesiak D, AlMangour B, Borkar T. Effect of energy density and scanning strategy on densification, microstructure and mechanical properties of 316L stainless steel processed via selective laser melting. *Mater Sci Eng A.* 2020;770:138455.
10. AlMangour B, Grzesiak D, Borkar T, Yang J-M. Densification behavior, microstructural evolution, and mechanical properties of TiC/316L stainless steel nanocomposites fabricated by selective laser melting. *Mater Des.* 2018;138:119-28.
11. AlMangour B, Grzesiak D, Cheng J, Ertas Y. Thermal behavior of the molten pool, microstructural evolution, and tribological performance during selective laser melting of TiC/316L stainless steel nanocomposites: experimental and simulation methods. *J Mater Process Technol.* 2018;257:288-301.
12. Khairallah SA, Anderson AT, Rubenchik A, King WE. Laser powder-bed fusion additive manufacturing: physics of complex melt flow and formation mechanisms of pores, spatter, and denudation zones. *Acta Mater.* 2016;108:36-45.
13. Yan W, Lin S, Kafka OL, Lian Y, Yu C, Liu Z, et al. Data-driven multi-scale multi-physics models to derive process-structure-property relationships for additive manufacturing. *Comput Mech.* 2018;61(5):521-41.
14. Tang C, Le KQ, Wong CH. Physics of humping formation in laser powder bed fusion. *Int J Heat Mass Transf.* 2020;149:119172.
15. Xia M, Gu D, Yu G, Dai D, Chen H, Shi Q. Porosity evolution and its thermodynamic mechanism of randomly packed powder-bed during selective laser melting of Inconel 718 alloy. *Int J Mach Tools Manuf.* 2017;116:96-106.
16. Tang C, Tan JL, Wong CH. A numerical investigation on the physical mechanisms of single track defects in selective laser melting. *Int J Heat Mass Transf.* 2018;126:957-68.
17. Ansari P, Rehman AU, Pitir F, Veziroglu S, Mishra YK, Aktas OC, et al. Selective laser melting of 316l austenitic stainless steel: detailed process understanding using multiphysics simulation and experimentation. *Metals.* 2021;11(7):1076.
18. Bayat M, Mohanty S, Hattel JH. Multiphysics modelling of lack-of-fusion voids formation and evolution in IN718 made by multi-track/multi-layer L-PBF. *Int J Heat Mass Transf.* 2019;139:95-114.
19. Zhang Y, Zhang J. Modeling of solidification microstructure evolution in laser powder bed fusion fabricated 316L stainless steel using combined computational fluid dynamics and cellular automata. *Addit Manuf.* 2019;28:750-65.
20. Luo Z, Zhao Y. Numerical simulation of part-level temperature fields during selective laser melting of stainless steel 316L. *Int J Adv Manuf Technol.* 2019;104(5-8):1615-35.
21. Cao L. Mesoscopic-scale simulation of pore evolution during laser powder bed fusion process. *Comput Mater Sci.* 2020;179:109686.
22. Liang Z, Zhirnov I, Zhang F, Jones KK, Deisenroth D, Williams M, et al. Development of computational framework for titanium alloy phase transformation prediction in laser powder-bed fusion additive manufacturing. *Materialia.* 2020;14:100934.
23. He Q, Xia H, Liu J, Ao X, Lin S. Modeling and numerical studies of selective laser melting: multiphase flow, solidification and heat transfer. *Mater Des.* 2020;196:109115.
24. Zhang X, Chen L, Zhou J, Ren N. Simulation and experimental studies on process parameters, microstructure and mechanical properties of selective laser melting of stainless steel 316L. *J Braz Soc Mech Sci Eng.* 2020;42(8):402.
25. Yu T, Zhao J. Semi-coupled resolved CFD-DEM simulation of powder-based selective laser melting for additive manufacturing. *Comput Methods Appl Mech Eng.* 2021;377:113707.
26. Moges T, Yang Z, Jones K, Feng S, Witherell P, Lu Y. Hybrid modeling approach for melt-pool prediction in laser powder bed fusion additive manufacturing. *J Comput Inf Sci Eng.* 2021;21(5):050902.
27. Kazemi Z, Soleimani M, Rokhgireh H, Nayebi A. Melting pool simulation of 316L samples manufactured by Selective Laser Melting method, comparison with experimental results. *Int J Therm Sci.* 2022;176:107538.
28. Zhang B, Liao H, Coddet C. Selective laser melting commercially pure Ti under vacuum. *Vacuum.* 2013;95:25-9.
29. King WE, Barth HD, Castillo VM, Gallegos GF, Gibbs JW, Hahn DE, et al. Observation of keyhole-mode laser melting in laser powder-bed fusion additive manufacturing. *J Mater Process Technol.* 2014;214(12):2915-25.
30. Anderson JD Jr. Governing equations of fluid dynamics. In: *Wendt JF, editor. Computational fluid dynamics: an introduction.* Berlin: Springer; 1992. p. 15-51.
31. *Fluent A. ANSYS fluent 12.0 theory guide.* Canonsburg, PA: ANSYS Inc.; 2009.

32. Versteeg HK, Malalasekera W. An introduction to computational fluid dynamics: the finite volume method. Harlow: Pearson Education; 2007.
33. Kik T. Heat source models in numerical simulations of laser welding. *Materials*. 2020;13(11):2653.
34. Zhang Z, Huang Y, Rani Kasinathan A, Imani Shahabad S, Ali U, Mahmoodkhani Y, et al. 3-Dimensional heat transfer modeling for laser powder-bed fusion additive manufacturing with volumetric heat sources based on varied thermal conductivity and absorptivity. *Opt Laser Technol*. 2019;109:297-312.
35. Liu S, Zhu H, Peng G, Yin J, Zeng X. Microstructure prediction of selective laser melting AlSi10Mg using finite element analysis. *Mater Des*. 2018;142:319-28.
36. Hasan A. CFD modelling of friction stir welding (FSW) process of AZ31 magnesium alloy using volume of fluid method. *J Mater Res Technol*. 2019;8(2):1819-27.
37. Dellinger G, Garambois P-A, Dellinger N, Dufresne M, Terfous A, Vazquez J, et al. Computational fluid dynamics modeling for the design of Archimedes Screw Generator. *Renew Energy*. 2018;118:847-57.
38. Mills KC. Recommended values of thermophysical properties for selected commercial alloys. Cambridge: Woodhead Publishing; 2002.
39. Hozoorbakhsh A, Ismail MIS, Aziz NBA. A computational analysis of heat transfer and fluid flow in high-speed scanning of laser micro-welding. *Int Commun Heat Mass Transf*. 2015;68:178-87.
40. Li C-J, Tsai T-W, Tseng C-C. Numerical simulation for heat and mass transfer during selective laser melting of titanium alloys powder. *Phys Procedia*. 2016;83:1444-9.
41. ANSYS, Inc. ANSYS meshing user's guide. Canonsburg, PA: ANSYS Inc.; 2010. p. 724-46.
42. Larimian T, AlMangour B, Grzesiak D, Walunj G, Borkar T. Effect of laser spot size, scanning strategy, scanning speed, and laser power on microstructure and mechanical behavior of 316L stainless steel fabricated via selective laser melting. *J Mater Eng Perform*. 2022;31(3):2205-24.